Extreme Mechanics Letters 85 (2026) 102482

Contents lists available at ScienceDirect

Extreme Mechanics Letters

journal homepage: www.elsevier.com/locate/eml

Hydrobraille: Water-responsive tactile surface morphing

Seokmin Moon [a], Kanghyun Ki [b,1], Uijin Oh [a], Yunseok Choi [a], Taehun Chung [c], Youn Soo Kim [c], Anna Lee [b], Jungil Choi [a,*], Jonghyun Ha [a,*]

[a] Department of Mechanical Engineering, Ajou University, Suwon 16499, Republic of Korea
[b] Department of Mechanical Engineering, Pohang University of Science and Technology, Pohang 37673, Republic of Korea
[c] Department of Materials Science and Engineering, Pohang University of Science and Technology, Pohang 37673, Republic of Korea

ARTICLE INFO

Keywords:
Hygroscopic swelling
Braille
Tactile surface
Soft materials

ABSTRACT

Surfaces capable of morphing offer transformative opportunities in adaptive interfaces, sensing, and soft robotics, yet achieving substantial, reversible deformation without external energy remains challenging. Among various approaches, moisture-responsive systems are particularly attractive because environmental humidity and liquid water are abundant energy sources. Here, we introduce hydrobraille, a moisture-responsive tactile platform wherein hygroscopic hydrogels embedded beneath a thin elastomeric membrane expand upon absorbing environmental moisture, driving controlled surface protrusions. Discrete hydrogel domains patterned in micromachined channels enable programmable deformation, guided by a scaling model that robustly captures experimental observations across varied geometries and material parameters. This simple power-free approach reliably operates through repeated wet-dry cycles and can be fabricated in a scalable and adaptable manner across various sizes and geometries. By harnessing ubiquitous moisture for mechanical actuation and tactile feedback, our platform expands the design landscape for applications including haptics, wearable sensors, biomedical devices, microfluidic systems, architectural skins, and environmental management.

1. Introduction

Tactile surfaces that dynamically alter their morphology provide a direct physical interface between humans and materials, enabling information exchange through touch. To realize tactile morphing, a variety of actuation strategies have been developed. Field-driven systems, including magnetic [1–3] and electroactive [4–6] approaches, enable rapid and programmable deformation but require coils, electrodes, and insulation circuits that increase power consumption and structural complexity. Pneumatic [7–9] and thermally responsive [10–12] strategies rely on air pressure or localized heating; however, pneumatic systems depend on pumps and valves that hinder portability, while thermally driven materials exhibit high energy demand for heating and temperature regulation. Although these active systems offer high spatial resolution and repeatable deformation, their dependence on continuous external power and control hardware restricts scalability and integration into flexible or wearable devices.

We introduce hydrobraille, a water-responsive tactile platform that transforms its surface through the volumetric swelling of hydrogels confined beneath an elastic membrane. Upon exposure to aqueous liquids, the hydrogel expands and generates localized protrusions through the mechanical interplay with the overlying membrane, converting the energy of water absorption into mechanical deformation without external power or control electronics. By integrating simple microfluidic architectures, the platform enables precise control over liquid flow paths and localized actuation, a level of control that is uncommon in material-driven tactile systems.

Building on this mechanism, we demonstrate versatile functionalities beyond conventional Braille (Fig. 1a), including tactile graphics, a sweat-sensing wearable patch, a capillary-valve-integrated fluid pressure sensor, and a condensation detection surface. These demonstrations highlight the potential of hydrobraille as a broad platform for fluid-responsive, material-driven tactile interfaces.

* Corresponding authors.
E-mail addresses: cji@ajou.ac.kr (J. Choi), hajh@ajou.ac.kr (J. Ha).
[1] Advanced Aeroengine Research Team, Korea Aerospace Research Institute, Daejeon 34133, Republic of Korea

https://doi.org/10.1016/j.eml.2026.102482
Received 23 February 2026; Received in revised form 23 March 2026; Accepted 15 April 2026
Available online 18 April 2026

2. Results and discussion

2.1. Working principle

Hydrobraille comprises spherical hydrogel beads embedded within microchannels, sealed by an elastic membrane. The system is initially flat in the dry state, but upon wetting, the hydrogel beads absorb moisture and swell, pushing against the elastic layer to form localized protrusions on the surface (Fig. 1b). These protrusions are mechanically comparable to standard Braille dots, allowing tactile recognition by human touch, as illustrated in Fig. 1c. The swelling is driven by the diffusion of water molecules into the hydrophilic hydrogel network [13, 14], resulting in an out-of-plane bulging of the membrane. Furthermore, as shown in Fig. 1d, the spatial configuration of raised dots can be precisely controlled by adjusting the wetted length within the channel. Sequential actuation of individual hydrogel sites enables programmable Braille patterns, simply by modulating the fluid injection into the inlet and the arrangement of hydrogel units along the microchannel.

By customizing the spatial configuration of hydrogel units within our Braille system, a diverse range of textual information can be encoded. Such customization is readily achieved through a simple fabrication process involving direct placement of hydrogel beads into microchannels, followed by membrane sealing, enabling rapid prototyping of various hydrobraille layouts (Fig. 1e). We provide the detailed fabrication process in Supplementary Material S1.

Building upon this design flexibility, we implement a proof-of-concept hydrobraille display integrated with a selective fluidic control system that individually supplies liquid to specific hydrogel chambers. This configuration allows on-demand actuation of chosen dots, enabling dynamic generation of Braille characters that function analogously to conventional electromechanical Braille displays. The system successfully reproduces distinct tactile patterns corresponding to different letters, confirming its potential as a reconfigurable and passively powered tactile communication interface (see Fig. 1f and Video S1).

Supplementary material related to this article can be found online at doi:10.1016/j.eml.2026.102482.

2.2. Energy equation of extrusion height

The extrusion height of the Braille dot (denoted as δ) is a key

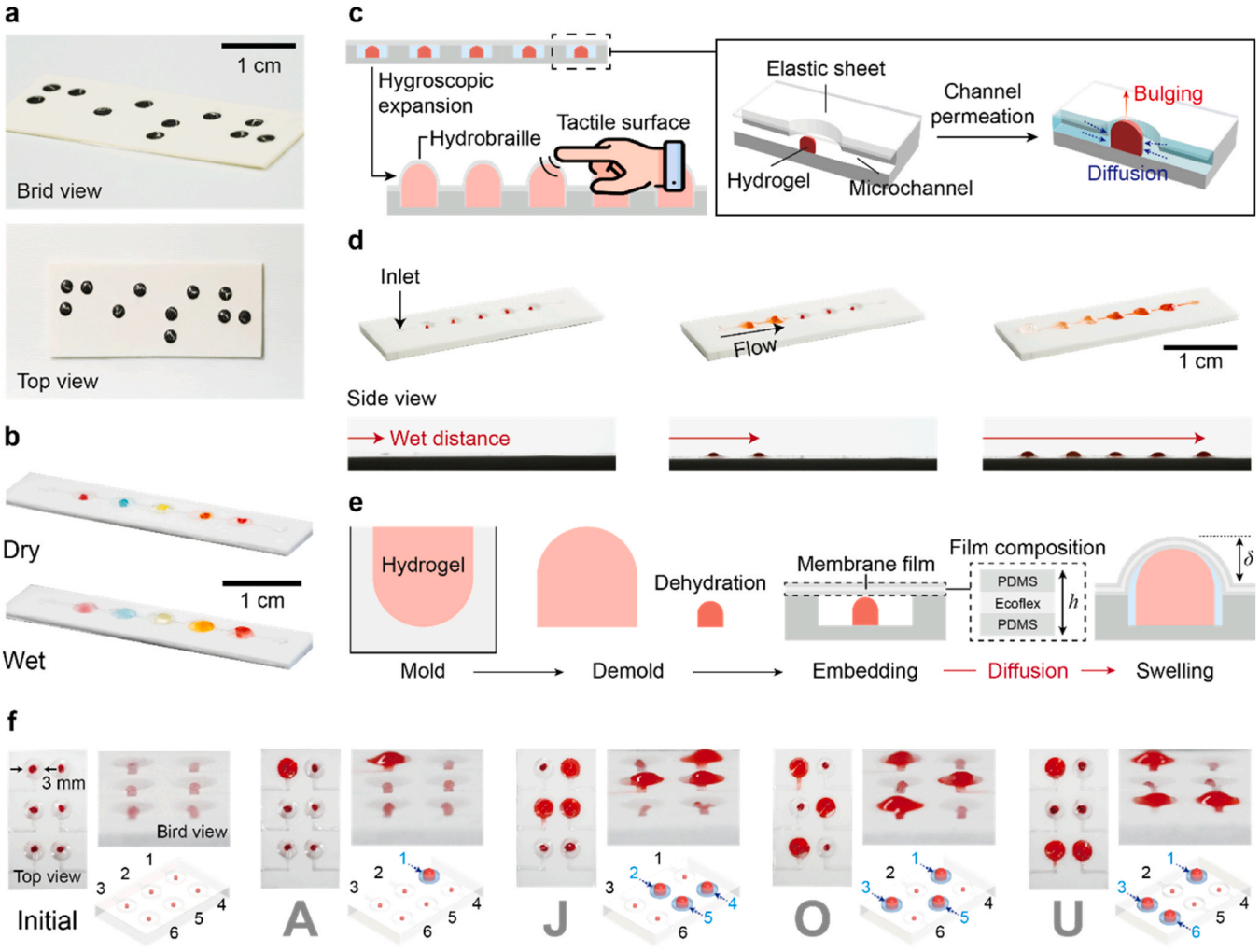

Fig. 1. Basic principle of hydrobraille tactile morphing. (a) Photograph of a conventional paper-based Braille sheet. Braille word represents 'fish.' (b) Optical images of the hydrobraille platform in the dry (upper) and hydrated (lower) states, showing emergence of tactile dots. (c) Schematic of the working principle in which hydrogel beads embedded in microchannels absorb water, swell, and push the overlying elastic membrane upward to form tactile protrusions. (d) Experimental results of fluid-induced actuation. The wetted length within the channel (represented by red arrows) determines the spatial activation of hydrogel swelling and the resulting Braille pattern formation. (e) Fabrication process of hydrobraille, including hydrogel molding, integration into microchannels, and membrane sealing. The sequence highlights dehydration, embedding, and subsequent swelling that drives tactile extrusion. The dashed box indicates the tri-layer membrane structure and its material composition. (f) Operation of hydrobraille as an active Braille display. By selectively pressurizing fluidic inlets, raised liquid domes form to represent the Braille characters A, J, O, and U, demonstrating a reconfigurable tactile display.

parameter that directly governs tactile detectability. In the hydrobraille system, δ arises from the mechanical interaction between the swelling of hydrogel beads and the tensile constraint imposed by the overlying elastic PDMS sheet. To analyze this interaction quantitatively, we develop a mechanical framework based on the total elastic energy of the system, incorporating both the deformation of the stretched membrane and the compressed hydrogel. As illustrated in Fig. 2a, water absorption leads to isotropic swelling of the hydrogel, but this expansion is vertically constrained by the PDMS sheet, resulting in localized bulging of the membrane. The system reaches an equilibrium state where δ is determined by the balance between the stored elastic energy in the stretched PDMS film and the strain energy of the compressed hydrogel. Using this energy-based approach, we derive a theoretical expression to predict δ as a function of material properties and geometric parameters.

Upon swelling, the hydrogel exerts a normal force on the overlying PDMS sheet, leading to its radial stretching (red box in Fig. 2a). The corresponding elastic energy stored in the film, e_f, arises from the in-plane deformation of the membrane and can be approximated as $e_f \sim E_f \varepsilon_f A_f \Delta R_c$, where E_f, ε_f, A_f, and ΔR_c represent the Young's modulus of the film, in-plane strain, cross-sectional area, and elongation of the film, respectively (see detailed derivation in Supplementary Material S2). Assuming the film deforms over the contact area of the hydrogel, the cross-sectional area can be estimated as $A_f \sim R_c h$, where R_c is the radius of the channel occupied by the hydrogel and h is the film thickness. The radial strain in the film is given by $\varepsilon_f \sim \Delta R_c / R_c$. Geometric considerations yield the film elongation as $\Delta R_c \sim (R_c^2 + \delta^2)^{1/2} - R_c$, where δ is the bulge height of the membrane. This expression captures the coupling between the swelling-induced vertical displacement and the lateral stretching of the elastic sheet.

While this swelling of the hydrogel induces radial stretching of the overlying elastic film, the film in turn imposes a compressive constraint on the hydrogel, resulting in the mechanical equilibrium between the two components (see the blue box in Fig. 2a). The elastic energy stored in the compressed hydrogel, denoted as e_h, can be approximated as $e_h \sim E_h \varepsilon_h A_h \delta^*$, where E_h, ε_h, A_h, and δ^* represent the Young's modulus of the hydrogel, compressive strain, cross-sectional area, and vertical deformation of the hydrogel, respectively (see detailed derivation in Supplementary Material S2). The cross-sectional area of the swollen hydrogel is estimated as $A_h \sim [R(1+s)]^2$, where R is the initial radius of the hydrogel and s is the swelling strain corresponding to the fully saturated state. For reliable Braille formation, we adopt a bullet-shaped hydrogel geometry with a height-to-radius ratio defined by a dimensionless design coefficient α, such that the initial hydrogel height is given by $d \sim \alpha R$. In our current design, we use $\alpha = 1.8$ (Fig. S2a). The compressive strain is then expressed as $\varepsilon_h \sim \delta^* / [\alpha R(1+s)]$, where the vertical compression is defined as $\delta^* \sim \alpha R s - \delta$. This framework allows us to understand the interplay between hydrogel geometry, swelling behavior, and the resulting mechanical response under confinement by the film.

The total elastic energy of the system is composed of two primary contributions: the stretching energy of the membrane film, e_f, and the compressive energy of the swollen hydrogel, e_h. At mechanical equilibrium, the system minimizes this total energy with respect to the extrusion height δ, leading to the condition:

$$\frac{\partial (e_f + e_h)}{\partial \delta} = 0 \tag{1}$$

Substituting the expressions for e_f and e_h derived above, the balance equation reflects the competition between the elastic resistance of the film to stretching and the compression of the swollen hydrogel. Solving this condition provides a theoretical prediction for δ as a function of materials (E_f, E_h), geometric parameters (R, h, α), and the swelling ratio s. Since Eq. (1) takes the form of a quartic polynomial in δ, an analytical solution is not straightforward. We therefore numerically solved the

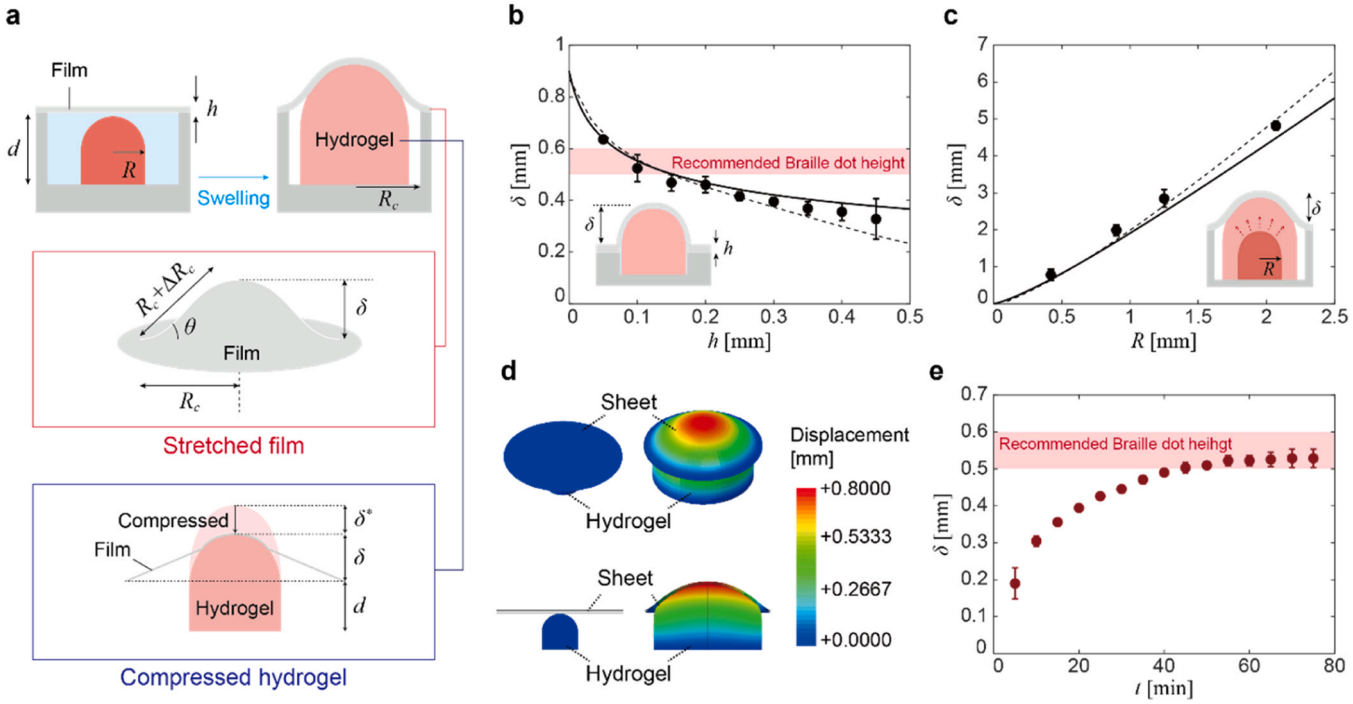

Fig. 2. Mechanical analysis of hydrobraille. **(a)** Schematic illustrating how hydrogel swelling produces the extrusion height, δ. The swollen hydrogel is laterally confined by the channel, forcing the elastic film to bulge upward (red box) while the hydrogel underneath becomes compressed (blue box). The interplay of hydrogel expansion and film stretching determines the Braille dot height. **(b)** Extrusion height as a function of film thickness, h, under fixed hydrogel size conditions. The solid line indicates theoretical predictions obtained by solving Eq. (1), while the dashed line represents the simulation result. **(c)** Extrusion height as a function of hydrogel radius, R, under fixed film thickness conditions, which is 0.1 mm. The solid line represents the theoretical height calculated from Eq. (1), and the dashed line is the height obtained by simulation. **(d)** Simulation of hydrobraille dot formation from bird and cross-sectional views ($R = 0.5$ mm, $h = 0.1$ mm). **(e)** Temporal evolution of extrusion height, δ, during the swelling process. The pink shaded band in Fig. b and e represents the recommended Braille height range of 0.5–0.6 mm [15,16].

equation to obtain δ under various conditions. The detailed process for deriving the differential equation, along with the numerical procedure used to solve it for δ, is provided in Supplementary Material S2.

2.3. Mechanical validation and swelling dynamics

We experimentally measure the extrusion height of the Braille dot (δ) across a range of membrane film thicknesses (Fig. 2b). The film thickness, h, is systematically varied from 50 to 450 μm by adjusting the spin-coating speed, with specific conditions summarized in Table S1. Microchannels are fabricated with a channel radius $R_c = 1.5$ mm, depth $d = 0.6$ mm, and hydrogel radius $R = 0.33$ mm. As the film thickness increases, the measured extrusion height gradually decreases, which is attributed to the enhanced bending stiffness of the elastic film. To evaluate the validity of the mechanical model, we numerically solve Eq. (1) using the corresponding experimental parameters. The theoretical predictions show close agreement with the measured values across the full thickness range (Fig. 2b). According to accessibility standards [15,16], a Braille dot height of at least 0.5–0.6 mm is required for effective tactile recognition, as indicated by the shaded pink region in the figure. Among the tested conditions, the film with $h = 100$ μm produces an extrusion height that reliably meets this tactile requirement. Accordingly, we adopt a film thickness of 100 μm for the hydrobraille system.

We further evaluate the robustness of the model by investigating how the extrusion height varies with different hydrogel sizes. To ensure consistency across experiments, we maintain a fixed ratio between the channel radius and hydrogel radius, approximated as $R_c \sim 3.5\,R$, based on the measured geometric relationship shown in Fig. S2b. As the hydrogel radius increases, the corresponding extrusion height also increases (Fig. 2c). The theoretical model described by Eq. (1) is corroborated by the experimental results, with slight deviations observed at larger hydrogel sizes due to the effective area correction not fully captured in the simplified model. Finite element simulations show even closer agreement with the experiments (dashed lines in Figs. 2b and 2c). Representative simulation images are shown in Fig. 2d, with methodology detailed in Supplementary Material S3.

The temporal evolution of the extrusion height is shown in Fig. 2e, where the hydrogel undergoes rapid initial swelling followed by gradual saturation. The characteristic diffusion time can be estimated as $\tau \sim Rs^2/D \sim 1000$ s, where D is the poroelastic diffusivity estimated from representative PAAm hydrogel parameters [17–20], consistent with the experimental observation (see Supplementary Material S4). The swelling rate is further modulated by solvent viscosity and temperature (Fig. S3), confirming that the dynamics are governed by diffusion-limited transport. Notably, increasing solvent viscosity also reduces the equilibrium swelling height due to inhibited polymerization of PAAm [21]. Details of the viscosity and temperature dependence are provided in Supplementary Material S4.

2.4. Hydrogel swelling–driven tactile graphics

The size-dependent deformation of hydrobraille enables the

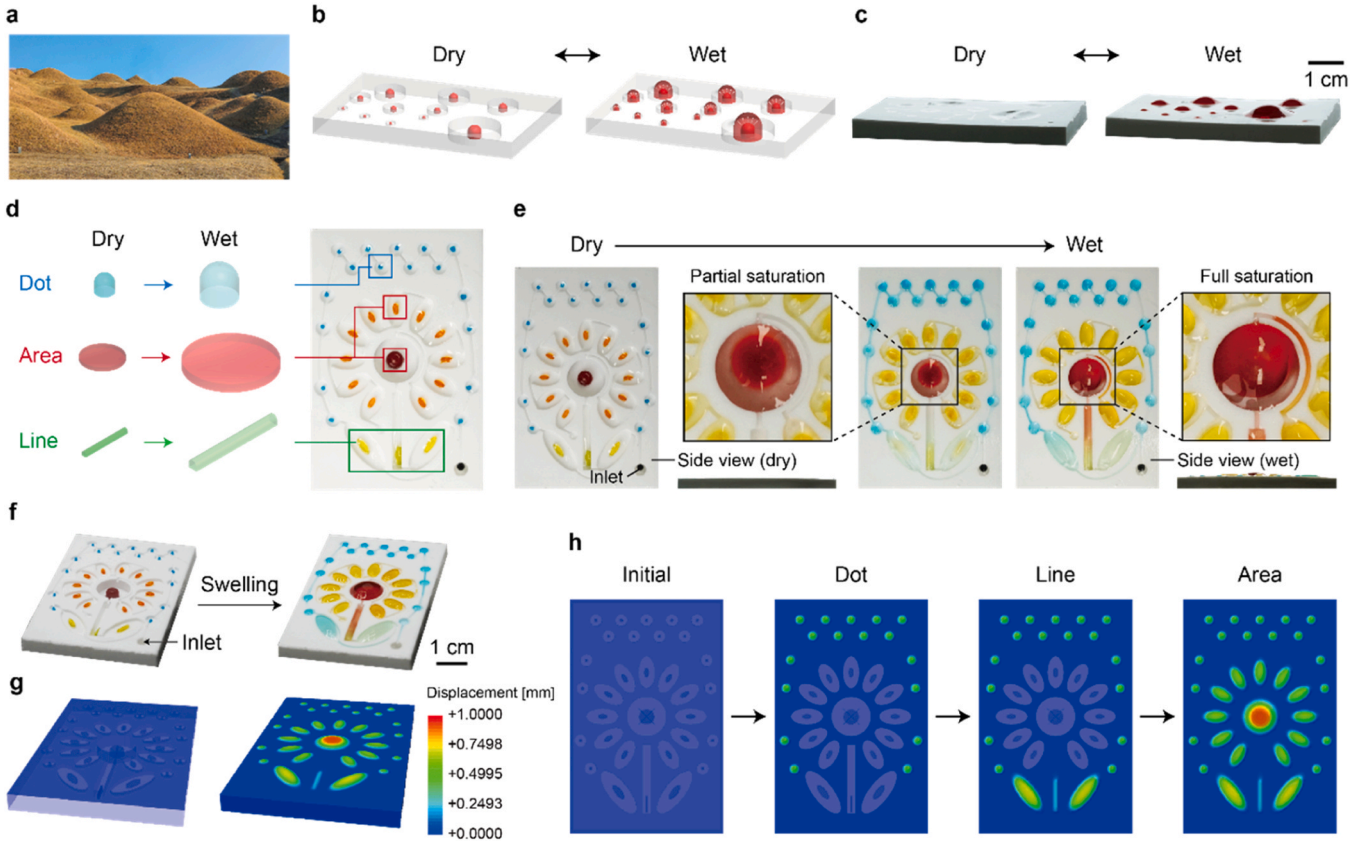

Fig. 3. Hydrogel-actuated tactile graphics. **(a)** Reference image of Korean ancient tombs (Dareungwon Ancient Tomb Complex, Gyeongju, Republic of Korea). **(b)** Schematic illustration of a dynamic morphing surface designed to emulate the topography of natural hill-like mounds, enabled by the swelling of hydrogels with varying sizes. **(c)** Experimental images demonstrating the realization of the schematic concept in Fig. 3b, showing mound-like tactile structures generated through size-dependent hydrogel swelling. **(d)** Hydrobraille components with distinct geometries (dot, line, and area) serving as basic building blocks for constructing tactile graphics, here assembled to represent a sunflower pattern. **(e)** Images showing the progression of the sunflower tactile graphic formation. Initially, all hydrogel components are wetted and begin to swell, forming tactile protrusions upon full saturation. The inset boxes indicate the central hydrogel before and after saturation. **(f)** Experimental images of a dynamically morphing flower-shaped tactile graphic, induced by swelling of hydrogels with varied geometries. **(g, h)** Simulated tactile morphing of a flower-shaped surface, shown from bird view (g) and top-down view (h).

construction of tactile graphics. Because the extrusion height is governed by the geometry and size of the hydrogel, the surface morphology can be tuned by spatially patterning hydrogel units of varying dimensions. The approach is well-suited for a range of tactile representations, including topographic features, symbolic contours, and educational graphics. We demonstrate this concept by constructing a tactile surface that mimics the contour of a traditional Korean tomb (Fig. 3a). Upon hydration, hydrogels of varying radii are modeled in 3D to illustrate the formation of a raised topography (Fig. 3b), and this effect is experimentally realized in practice, where the swollen hydrogels produce protrusions that flatten back to a smooth surface upon drying (Fig. 3c).

To further illustrate the versatility of this approach, we fabricate a flower-shaped tactile surface composed of three distinct hydrogel geometries (dot, line, and area) embedded within a PDMS microchannel molded in a floral layout (Fig. 3d). Upon wetting, all hydrogel

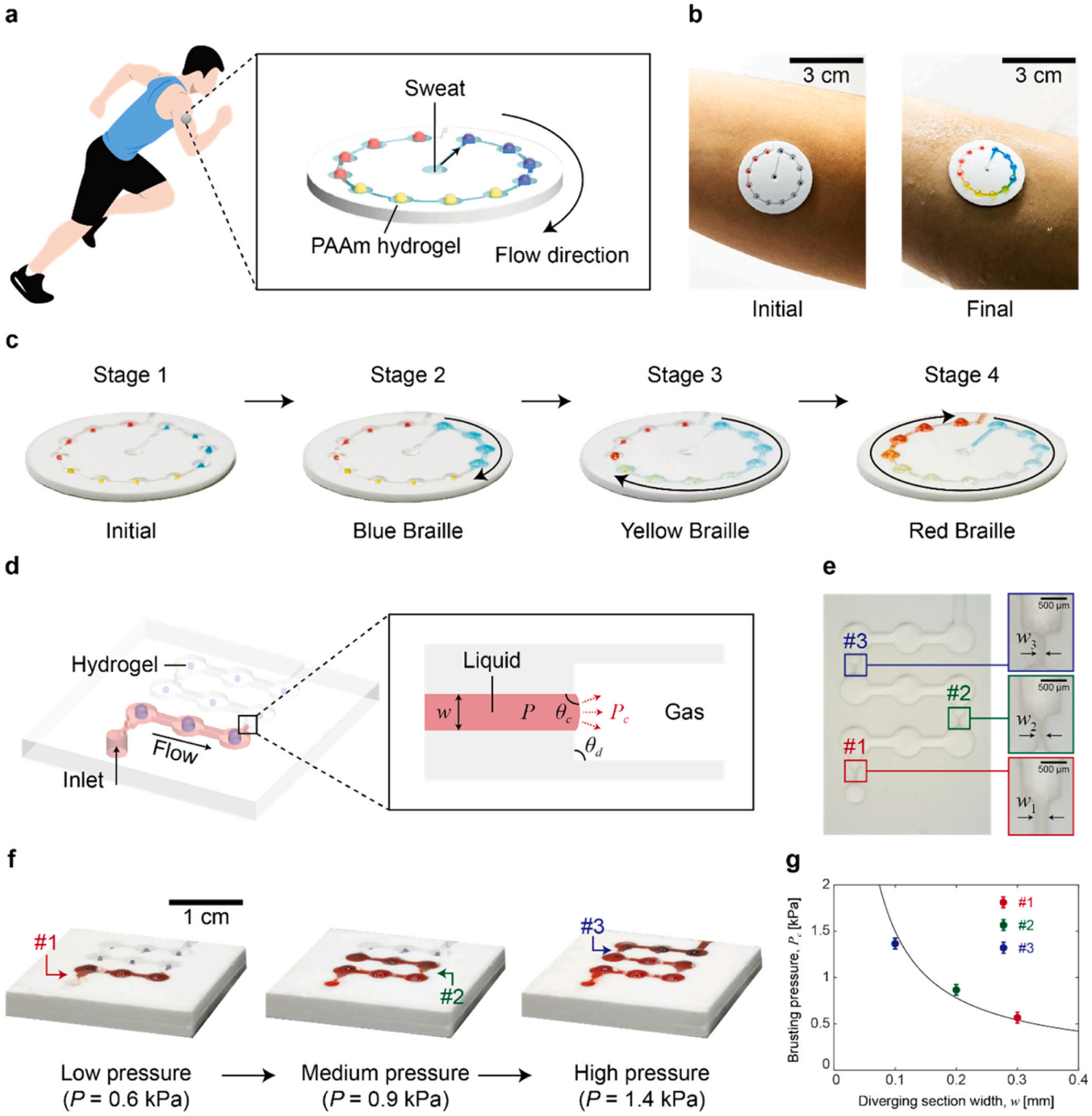

Fig. 4. Wearable applications of hydrobraille. **(a)** Schematic showing the structural design and working principle of the sweat-capturing patch, which utilizes swelling of hydrogel. **(b)** Experimental images of sweat capture and resulting tactile protrusions on the patch surface. **(c)** Sequential images showing progressive hydrogel swelling corresponding to increasing sweat accumulation. **(d)** Schematic of the tactile pressure sensor integrating capillary bursting valves (CBVs) with hydrogel swelling. The black box shows the CBV channel design. **(e)** Optical image of microchannel, featuring three distinct CBV sections defined by channel widths of $w_1 = 0.3$ mm, $w_2 = 0.2$ mm, and $w_3 = 0.1$ mm. **(f)** Experimental images showing pressure-dependent formation of tactile dots corresponding to the sequential activation of CBV regions at increasing flow pressures. **(g)** Experimentally measured bursting pressures. The solid line corresponds to the theoretically predicted pressure thresholds, P_c.

components start from a fully hydrated state and subsequently swell at different rates depending on their size. Smaller geometries exhibit faster swelling and reach a fully swollen state due to shorter diffusion lengths, while larger units swell more slowly, resulting in a progressive formation of the surface (Fig. 3e and f). We also perform numerical simulations to replicate the three-dimensional surface transformation of the flower-shaped tactile graphic. The simulated displacement fields shown closely capture the experimentally observed swelling behavior (Fig. 3g and h). By assigning appropriate initial geometries and boundary conditions, the simulation accurately reproduces the progressive surface protrusion pattern resulting from differential swelling. This computational approach provides a predictive framework for designing complex tactile graphics before fabrication. Details of the simulation methodology are provided in Supplementary Material S3.

2.5. Touch-responsive wearable patch for sweat visualization

As an extension of the tactile graphic concept, the hydrobraille platform is applicable to sweat-responsive sensing patches that provide nonvisual feedback. The patch employs the same hydrogel-microchannel architecture. The operation mechanism is illustrated in Fig. 4a, where sweat flows inward from a central inlet and gradually permeates the microchannel. As sweat reaches each hydrogel unit, sweat absorption induces swelling, which deforms the overlying membrane to produce localized surface protrusions that can be clearly felt by touch. During exercise, physiological conditions such as hydration can change rapidly, making real-time self-monitoring important, as rapid fluctuations in hydration may lead to dehydration-related risks. This capability is particularly valuable for visually impaired individuals, who face accessibility limitations not encountered by sighted users. Most existing real-time wearable sensors, including commercial smartwatches and colorimetric sweat patches, rely exclusively on visual readouts that are not accessible to visually impaired users [22–24]. In contrast, our system allows users to confirm sweat capture in real-time through tactile feedback, thereby enhancing accessibility for visually impaired individuals. It also remains effective in situations where visual observation is limited, such as nighttime use or when worn beneath clothing.

Fig. 4b shows the patch applied to the forearm before and after exercise. In the dry state, the surface remains smooth. As sweat accumulates and flows outward, sequential protrusions emerge along the channel path, providing tactile confirmation of fluid collection. To map the level of perspiration in a way that is both spatially and perceptually distinct, we dye the hydrogel units in blue, yellow, and red and arrange them in that order along the flow path. As shown in the time-lapse sequence of Fig. 4c and Fig. S4, the blue hydrogels swell first, followed by yellow and finally red hydrogels as the sweat volume increases. This staged actuation correlates with sweat accumulation, reflecting both the intensity and duration of exercise, and could potentially be used to provide hydration guidelines. All experiments were performed in accordance with the guidelines of the institutional review board of Ajou University (202410-HS-002) and approved by the ethics committee at Ajou University.

2.6. Capillary-guided tactile fluid pressure sensor

The microfluidic architecture underlying the hydrobraille platform enables its direct adaptation to fluid pressure-responsive applications by incorporating capillary bursting valves (CBVs). These passive fluid control elements are widely used in microfluidic systems because they allow tunable threshold pressures through geometric design alone, without requiring external actuation [25–27]. Here, we develop hydrobraille with integrated CBVs to create a tactile fluid pressure sensor that provides pressure readout through touch.

The device layout and working principle are illustrated in Fig. 4d. Fluid flows along the microchannel until it encounters CBVs, which arrest the flow unless the applied pressure exceeds their characteristic bursting thresholds. Once the pressure surpasses this threshold, the fluid moves forward and reaches the downstream hydrogel. The absorbed fluid causes the hydrogel to swell, deforming the overlying membrane and forming a tactile bump. Each bursting threshold is controlled by the width of the diverging section, w, and the channel depth, d. As described in prior works, the bursting pressure is approximated by $P_c = -2\gamma(\cos\theta_i/w + \cos\theta_c/d)$, where γ is the liquid surface tension, θ_c is the contact angle of the channel surface, θ_d is the diverging angle of the channel, and θ_i is the minimum of $(\theta_c + \theta_d, 180°)$ [28–30]. In this design, $d = 0.8$ mm and $\theta_d = 90°$, using $\theta_c \approx 110°$.

Three CBVs are fabricated with widths of 0.3 mm, 0.2 mm, and 0.1 mm, corresponding to calculated bursting pressures of approximately 0.5 kPa, 0.8 kPa, and 1.5 kPa. Fig. 4e shows the layout of the three valve segments with magnified insets highlighting the varying geometries. To validate the tactile pressure sensor, water dyed with red food coloring is injected into the system at incrementally increasing pressures. As shown in Fig. 4f, the first tactile response appears at 0.6 kPa, where valve #1 is breached. At 0.9 kPa, valve #2 is activated, and at 1.4 kPa, valve #3 is triggered. These experimentally observed bursting events are in close agreement with the theoretical predictions (Fig. 4g).

This pressure-responsive system provides a tactile modality for fluid pressure readout. Because the platform requires no electronics or power input, it can function in environments where conventional sensors are difficult to operate. Potential applications include monitoring the pressure of sweat exuded from the skin, as well as measuring flow pressures of light-sensitive liquids that are preferably handled without illumination. These examples illustrate the versatility of hydrobraille as a nonvisual sensing interface for both wearable healthcare monitoring and laboratory fluid handling.

2.7. Condensation detection and preventing dew run-off

Condensation on cold surfaces often leads to droplet accumulation that eventually drips downward, causing leakage and potential functional or safety issues (Fig. 5a). Such events are common on refrigerator doors, vehicle windows, and portable electronics, where uncontrolled water flow can hinder performance or usability. To address this issue, we adapt the hydrobraille system into a dew detection and mitigation patch by introducing a perforated membrane film (Fig. 5b). When placed on a cold surface, condensed droplets pass through the perforations and are absorbed by the underlying hydrogels (black box in Fig. 5b), which swell to form tactile protrusions that signal condensation.

To demonstrate this concept, we perform a simple experiment using a Peltier module operated continuously for 24 h to create sustained cooling. The entire setup is enclosed in a constant temperature and humidity chamber (S-TH252, SERIMA) to maintain stable environmental conditions. The surface temperature of the Peltier module is maintained at −5 °C, while the ambient environment is kept at 30 °C and 80% relative humidity. Under these conditions, dew condenses on the perforated surface (dashed box in Fig. 5c) and is absorbed by the embedded hydrogels, which swell to form tactile dots (see black box in Fig. 5c). Although part of the condensed water is not captured due to the finite absorption rate of the hydrogels, the system effectively reduces dripping compared to the control surfaces. To quantify this effect, we compare three configurations: a flat PDMS patch without perforations, a perforated PDMS patch without hydrogels, and the hydrobraille patch incorporating hydrogels beneath the perforated membrane (Fig. 5d). The uncaptured dew volume is measured for each configuration during continuous Peltier operation (Fig. 5e and Video S2). After 24 h, the hydrobraille patch retains approximately 12 mL more water than the flat PDMS patch without holes, confirming that the embedded hydrogels absorb condensed water and thereby substantially mitigate condensation-induced leakage. Further optimization of hydrogel composition and membrane porosity is expected to enhance both detection sensitivity and absorption efficiency, expanding its potential

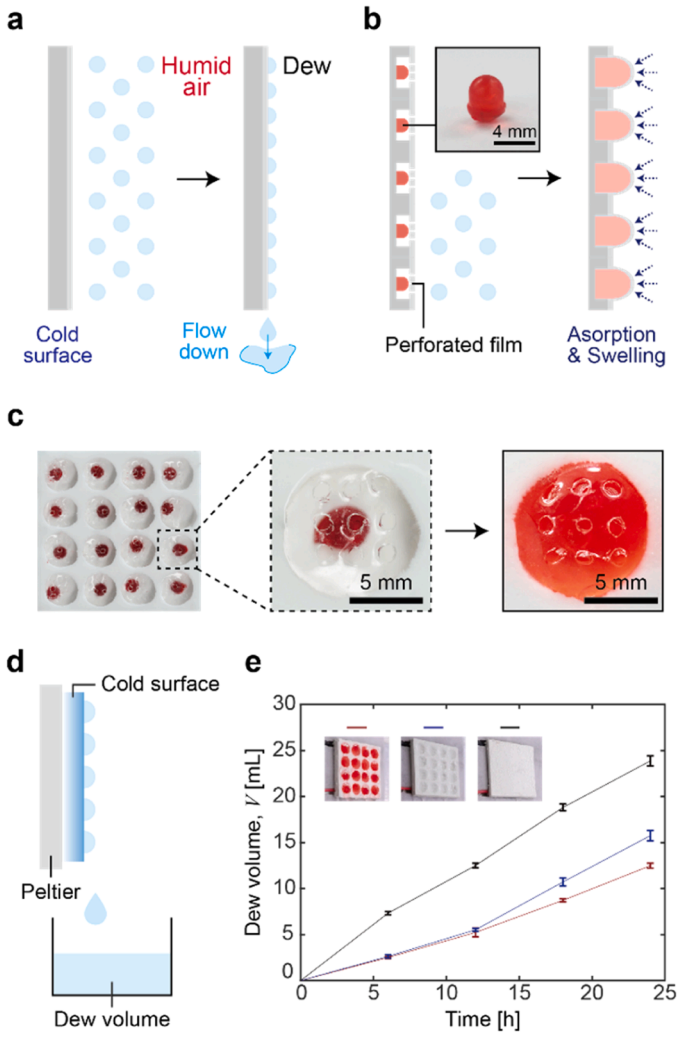

Fig. 5. Condensation-sensing hydrobraille preventing dew run-off. (a) Schematic of dew formation and droplet run-off on a cooled surface. (b) Schematic of the dew-sensing mechanism, in which hydrobraille absorbs condensed droplets and provides tactile feedback through hydrogel swelling. The black box shows a magnified view of an embedded hydrogel. (c) Experimental images of the patch. The dashed box indicates the perforated membrane, and the black box shows braille dot formation. (d) Schematic of the experimental setup. (e) Uncaptured dew volume, V, during Peltier operation for three configurations: hydrobraille patch (red), perforated PDMS without hydrogels (blue), and flat PDMS without perforations (black).

for practical applications in anti-fogging and moisture management surfaces.

Supplementary material related to this article can be found online at doi:10.1016/j.eml.2026.102482.

3. Conclusion

In summary, we presented a passive, water-responsive tactile system that harnesses the swelling behavior of hydrogels to produce localized surface protrusions. This platform, termed hydrobraille, consists of hydrogel elements embedded in microchannels and sealed with an elastic membrane. Upon moisture exposure, the hydrogels expanded and deformed the overlying film, forming tactile bumps. Through a combination of theoretical modeling, numerical simulation, and experimental measurements, we analyzed the overall mechanical behavior of the hydrobraille system and established a scaling framework that captured the extrusion height across varied geometric and material parameters.

We demonstrated the versatility of this system through a range of applications, including tactile graphics that morphed into symbolic and geometric shapes such as flowers and mound-like structures. Additional demonstrations included a sweat patch that provided intuitive tactile feedback based on fluid uptake, a pressure-responsive display integrated with capillary bursting valves for touch-based pressure readout, and a surface condensation sensor that detected and mitigated dew run-off. These examples highlighted the adaptability of hydrobraille as a self-actuating and programmable tactile interface suitable for diverse applications in communication, diagnostics, and environmental sensing.

Despite these capabilities, the current system has limitations that warrant further investigation. The response time, governed by diffusion-limited swelling kinetics, remained in the order of minutes, which may restrict applications requiring rapid tactile feedback. Strategies such as reducing hydrogel dimensions, engineering porous network architectures, or employing hydrogels with higher intrinsic diffusivity could substantially accelerate the actuation speed. For example, decreasing the crosslinker (MBAA) concentration increases the mesh size of the polymer network, thereby enhancing permeability and diffusivity [31,32]. In addition, introducing superporous architectures (~100 μm pores) via foaming reactions (e.g., $NaHCO_3$) can create interconnected porous network that significantly accelerates fluid transport [33,34]. These approaches provide viable routes to improve the actuation speed in future hydrobraille-based devices.

In addition to improving actuation speed, further investigation of long-term cyclic durability under repeated wet–dry conditions is necessary to ensure operational reliability for practical deployment. Future work will also explore the integration of bioresponsive hydrogel that selectively swells in response to target biomolecules, advancing hydrobraille as a platform for diagnostic kits capable of converting biochemical recognition into tactile signals for accessible disease detection [35,36].

CRediT authorship contribution statement

Seokmin Moon: Writing – original draft, Visualization, Validation, Formal analysis. **Taehun Chung:** Formal analysis. **Yunseok Choi:** Investigation. **Uijin Oh:** Investigation. **Kanghyun Ki:** Software. **Jonghyun Ha:** Writing – review & editing, Writing – original draft, Supervision, Funding acquisition. **Jungil Choi:** Writing – review & editing, Writing – original draft, Supervision. **Anna Lee:** Methodology. **Youn Soo Kim:** Methodology.

Declaration of Competing Interest

The authors declare that they have no known competing financial interests or personal relationships that could have appeared to influence the work reported in this paper.

Acknowledgement

We are grateful to Dongjo Kim for providing the image of Dareungwon used in Fig. 3a.

This work was supported by the National Research Foundation of Korea (NRF) grant funded by the Korea government (No. RS-2024–00341444).

Appendix A. Supporting information

Supplementary data associated with this article can be found in the online version at doi:10.1016/j.eml.2026.102482.

Data availability

Data will be made available on request.

References

[1] J.J. Zárate, H. Shea, Using pot–magnets to enable stable and scalable electromagnetic tactile displays, IEEE Trans. Haptics 10 (2017) 106–112, https://doi.org/10.1109/TOH.2016.2591951.

[2] J. Kim, B.-K. Han, D. Pyo, S. Ryu, H. Kim, D.-S. Kwon, Braille display for portable device using flip–latch structured electromagnetic actuator, IEEE Trans. Haptics 13 (2020) 59–65, https://doi.org/10.1109/TOH.2019.2963858.

[3] A. Abbasi, T. Chen, B.F.G. Aymon, P.M. Reis, Leveraging the snap buckling of bistable magnetic shells to design a refreshable braille dot, Adv. Mater. Technol. 9 (2024) 2301344, https://doi.org/10.1002/admt.202301344.

[4] G. Frediani, H. Boys, M. Ghilardi, S. Poslad, J.J.C. Busfield, F. Carpi, A soft touch: wearable tactile display of softness made of electroactive elastomers, Adv. Mater. Technol. 6 (2021) 2100016, https://doi.org/10.1002/admt.202100016.

[5] X. Qu, X. Ma, B. Shi, H. Li, L. Zheng, C. Wang, Z. Liu, Y. Fan, X. Chen, Z. Li, Z. L. Wang, Refreshable braille display system based on triboelectric nanogenerator and dielectric elastomer, Adv. Funct. Mater. 31 (2021) 2006612, https://doi.org/10.1002/adfm.202006612.

[6] S.-Y. Jang, M. Cho, H. Kim, M. Choi, S. Mun, J.-H. Youn, J. Park, G. Hwang, I. Hwang, S. Yun, K.-U. Kyung, Dynamically reconfigurable shape–morphing and tactile display via hydraulically coupled mergeable and splittable PVC gel actuator, Sci. Adv. 10 (2024) eadq2024, https://doi.org/10.1126/sciadv.adq2024.

[7] X. Wu, S.-H. Kim, H. Zhu, C.-H. Ji, M.G. Allen, A refreshable braille cell based on pneumatic microbubble actuators, J. Micro Syst. 21 (2012) 908–916, https://doi.org/10.1109/JMEMS.2012.2190043.

[8] B. Mosadegh, A.D. Mazzeo, R.F. Shepherd, S.A. Morin, U. Gupta, I.Z. Sani, D. Lai, S. Takayama, G.M. Whitesides, Control of soft machines using actuators operated by a Braille display, Lab Chip 14 (2014) 189–199, https://doi.org/10.1039/C3LC51083B.

[9] B. Shan, C. Liu, Y. Gao, Y. Wang, W. Guo, Y. Zhang, A multi–layer stacked microfluidic tactile display with high spatial resolution, IEEE Trans. Haptics 17 (2024) 546–556, https://doi.org/10.1109/TOH.2024.3367708.

[10] I. Hwang, S. Mun, J.-H. Youn, H.J. Kim, S.K. Park, M. Choi, T.J. Kang, Q. Pei, S. Yun, Height–renderable morphable tactile display enabled by programmable modulation of local stiffness in photothermally active polymer, Nat. Commun. 15 (2024) 2554, https://doi.org/10.1038/s41467-024-46709-7.

[11] M. Linnander, D. Goetz, G. Reardon, V. Kumar, E. Hawkes, Y. Visell, Tactile displays driven by projected light, Sci. Robot 10 (2025) eadv1383, https://doi.org/10.1126/scirobotics.adv1383.

[12] A. Mazzotta, S. Taccola, I. Cesini, M.S. Sifuentes, R.A. Harris, V. Mattoli, Low–voltage wearable tactile display with thermo–pneumatic actuation, npj Flex. Electron 9 (2025) 70, https://doi.org/10.1038/s41528-025-00426-3.

[13] P. Kim, L.D. Zarzar, X. He, A. Grinthal, J. Aizenberg, Hydrogel-actuated integrated responsive systems (HAIRS): moving towards adaptive materials, Curr. Opin. Solid State Mater. Sci. 15 (2011) 236–245, https://doi.org/10.1016/j.cossms.2011.05.004.

[14] R. Foudazi, R. Zowada, I. Manas-Zloczower, D.L. Feke, Porous hydrogels: present challenges and future opportunities, Langmuir 39 (2023) 2092–2111, https://doi.org/10.1021/acs.langmuir.2c02253.

[15] Braille Authority of North America, “Size and spacing of braille characters”, ⟨https://brailleauthority.org/size-and-spacing-braille-characters⟩.

[16] UK Association for Accessible Formats, “Standard dimensions for the UK Braille cell”, ⟨https://www.ukaaf.org/wp-content/uploads/2020/03/Braille-Standard-Dimensions.pdf⟩.

[17] J. Yoon, S. Cai, Z. Suo, R.C. Hayward, Poroelastic swelling kinetics of thin hydrogel layers: comparison of theory and experiment, Soft Matter 6 (2010) 6004–6012, https://doi.org/10.1039/C0SM00434K.

[18] J.-F. Louf, S.S. Datta, Poroelastic shape relaxation of hydrogel particles, Soft Matter 17 (2021) 3840–3847, https://doi.org/10.1039/D0SM02243H.

[19] T. Boudou, J. Ohayon, C. Picart, P. Tracqui, An extended relationship for the characterization of Young's modulus and Poisson's ratio of tunable polyacrylamide gels, Biorheology 43 (2006) 721–728, https://doi.org/10.1177/0006355X2006043006005.

[20] J. Wang, J.C. Burton, Hyperelastic swelling of stiff hydrogels, Phys. Rev. Lett. 134 (2025) 148203, https://doi.org/10.1103/PhysRevLett.134.148203.

[21] C. Li, X. Deng, X. Zhou, Synthesis antifreezing and antidehydration organohydrogels: one-step in-situ gelling versus two-step solvent displacement, Polymers 12 (2020) 2670, https://doi.org/10.3390/polym12112670.

[22] L.B. Baker, J.B. Model, K.A. Barnes, M.L. Anderson, S.P. Lee, K.A. Lee, S.D. Brown, A.J. Reimel, T.J. Roberts, R.P. Nuccio, J.L. Bonsignore, C.T. Ungaro, J.M. Carter, W. Ii, M.S. Seib, J.T. Reeder, A.J. Aranyosi, J.A. Rogers, R. Ghaffari, Skin-interfaced microfluidic system with personalized sweating rate and sweat chloride analytics for sports science applications, Sci. Adv. 6 (2020) eabe3929, https://doi.org/10.1126/sciadv.abe3929.

[23] J. Kim, Y. Wu, H. Luan, D.S. Yang, D. Cho, S.S. Kwak, S. Liu, H. Ryu, R. Ghaffari, J. A. Rogers, A skin-interfaced, miniaturized microfluidic analysis and delivery system for colorimetric measurements of nutrients in sweat and supply of vitamins through the skin, Adv. Sci. 9 (2022) 2103331, https://doi.org/10.1002/advs.202103331.

[24] S. Cho, S.M. Shaban, R. Song, H. Zhang, D. Yang, M.-J. Kim, Y. Xiong, X. Li, K. Madsen, S. Wapnick, S. Zhang, Z. Chen, J. Kim, G. Guinto, M. Li, M. Lee, R. F. Nuxoll, S. Shajari, J. Wang, S. Son, J. Shin, A.J. Aranyosi, D.E. Wright, T.-I. Kim, R. Ghaffari, Y. Huang, D.-H. Kim, J.A. Rogers, A skin-interfaced microfluidic platform supports dynamic sweat biochemical analysis during human exercise, Sci. Transl. Med. 16 (2024) eado5366, https://doi.org/10.1126/scitranslmed.ado5366.

[25] D. Juncker, H. Schmid, U. Drechsler, H. Wolf, M. Wolf, B. Michel, N. de Rooij, E. Delamarche, Autonomous microfluidic capillary system, Anal. Chem. 74 (2002) 6139–6144, https://doi.org/10.1021/ac0261449.

[26] T.-S. Leu, P.-Y. Chang, Pressure barrier of capillary stop valves in micro sample separators, Sens. Actuators A Phys. 115 (2004) 508–515, https://doi.org/10.1016/j.sna.2004.02.036.

[27] K.H. Chung, J.W. Hong, D.-S. Lee, H.C. Yoon, Microfluidic chip accomplishing self-fluid replacement using only capillary force and its bioanalytical application, Anal. Chim. Acta 585 (2007) 1–10, https://doi.org/10.1016/j.aca.2006.12.012.

[28] A. Glière, C. Delattre, Modeling and fabrication of capillary stop valves for planar microfluidic systems, Sens. Actuators A Phys. 130 (2006) 601–608, https://doi.org/10.1016/j.sna.2005.12.011.

[29] H. Cho, H.-Y. Kim, J.Y. Kang, T.S. Kim, How the capillary burst microvalves work, J. Colloid Interface Sci. 306 (2007) 379–385, https://doi.org/10.1016/j.jcis.2006.10.077.

[30] J. Choi, D. Kang, S. Han, S.B. Kim, J.A. Rogers, Thin, soft, skin-mounted microfluidic networks with capillary bursting valves for chrono-sampling of sweat, Adv. Healthc. Mater. 6 (2017) 1601355, https://doi.org/10.1002/adhm.201601355.

[31] F. Milos, A. del Campo, Polyacrylamide hydrogels as versatile biomimetic platforms to study cell-materials interactions, Adv. Mater. Interfaces 11 (2024) 2400404, https://doi.org/10.1002/admi.202400404.

[32] J. Lei, Y. Gao, S. Xu, L. He, Z. Liu, The effect of the effective polymer network on the extremely large deformation and fracture behaviors of polyacrylamide hydrogels, J. Mech. Phys. Solids 200 (2025) 106124, https://doi.org/10.1016/j.jmps.2025.106124.

[33] J. Chen, H. Park, K. Park, Synthesis of superporous hydrogels: hydrogels with fast swelling and superabsorbent properties, J. Biomed. Mater. Res. 44 (1999) 53–62, https://doi.org/10.1002/(SICI)1097-4636(199901)44:1<53::AID-JBM6>3.0.CO;2-W.

[34] H. Choudhary, S.R. Raghavan, Superfast-expanding porous hydrogels: pushing new frontiers in converting chemical potential into useful mechanical work, ACS Appl. Mater. Interfaces 14 (2022) 13733–13742, https://doi.org/10.1021/acsami.2c00645.

[35] T. Miyata, N. Asami, T. Uragami, A reversibly antigen-responsive hydrogel, Nature 399 (1999) 766–769, https://doi.org/10.1038/21619.

[36] R. Zhang, A. Bowyer, R. Eisenthal, J. Hubble, A smart membrane based on an antigen-responsive hydrogel, Biotechnol. Bioeng. 97 (2007) 976–984, https://doi.org/10.1002/bit.21255.

Supplementary Material

Hydrobraille: Water-responsive tactile surface morphing

Seokmin Moon[a], Kanghyun Ki[b,1], Uijin Oh[a], Yunseok Choi[a], Taehun Chung[c], Youn Soo Kim[c], Anna Lee[b], Jungil Choi[a], and Jonghyun Ha[a*]*

[a] Department of Mechanical Engineering, Ajou University, Suwon 16499, Republic of Korea
[b] Department of Mechanical Engineering, Pohang University of Science and Technology, Pohang 37673, Republic of Korea
[c] Department of Materials Science and Engineering, Pohang University of Science and Technology, Pohang 37673, Republic of Korea

* Corresponding authors. Email: cji@ajou.ac.kr, hajh@ajou.ac.kr

[1] Advanced Aeroengine Research Team, Korea Aerospace Research Institute, Daejeon 34133, Republic of Korea

S1. Fabrication methods

S1.1. Synthesis of hydrogel

A polyacrylamide (PAAm) hydrogel precursor solution is prepared by dissolving 800 mg of acrylamide (AAm, CAS: 79-06-1), 7.75 mg of N,N'-Methylenebisacrylamide (MBAA, CAS: 110-26-9), and 15 mg of ammonium persulfate (APS, CAS: 7727-54-0) in 5 mL of deionized water. After complete dissolution, 3.9 mg of N,N,N',N'-Tetramethylethylenediamine (TEMED, CAS: 110-18-9) is added as an accelerator, and the solution is homogenized using a vortex mixer. The precursor solution is then cast into customized molds fabricated by 3D printing (Form 4, Formlabs) and allowed to polymerize at room temperature for 3 h. Following gelation, the hydrogel structures are demolded and dehydrated under ambient conditions, producing shrunken hydrogel components suitable for embedding in microchannels.

S1.2. Fabrication method of hydrobraille

The hydrobraille system is fabricated through a sequence of microchannel preparation, trilayer membrane formation, and final bonding of the two components.

Microchannels are first fabricated by spin-coating polydimethylsiloxane (PDMS, Sylgard 184; Vision Lab Sciences) with a base-to-curing agent ratio of 10:1, pre-mixed with a white pigment (Silc Pig^{TM}) for enhanced visibility, onto a lithographically patterned silicone wafer. The spin-coating process is performed at 100 rpm for 30 s, followed by thermal curing at 110 ℃ for 5 min. The resulting PDMS layer, with a uniform thickness of approximately 1 mm, is subsequently peeled off to yield the microchannel structure with an embedded channel depth of 0.6 mm.

To prepare the membrane film that overlays the hydrogel-embedded channels, we construct a trilayer structure consisting of a central layer of Ecoflex 00-30 (Smooth On Inc.) sandwiched between outer PDMS layers. First, a PDMS layer (Sylgard 184; 10:1 ratio) is spin-coated onto a flat silicon wafer at 3000 rpm for 30 s and thermally cured at 110 ℃ for 5 min to form the base layer. Ecoflex 00-30 (part A: part B = 1:1), pre-mixed using a planetary mixer (Paste Mixer, Daehwa Tech) at 500 rpm for 1 min, is then spin-coated directly onto the cured PDMS layer at 3000 rpm for 30 s and cured at 110 ℃ for 5 min to form the intermediate elastomeric layer. Finally, a second PDMS layer (10:1 ratio) is spin-coated onto the Ecoflex 00-30 surface under the same conditions, completing the trilayer membrane assembly. The overall thickness of the composite film is approximately 0.1 mm.

After peeling the microchannel, the exposed PDMS surface remains slightly under-cured and retains mild tackiness. We embed the hydrogel within the PDMS microchannels, where the tacky PDMS surface temporarily holds the hydrogel in place. This interfacial adhesion is further reinforced by oxygen plasma treatment applied to both the PDMS channel and the trilayer membrane prior to final assembly, which activates the surfaces and promotes robust covalent bonding between components.

Both the hydrogel-embedded PDMS channel and the trilayer membrane are treated with oxygen plasma (CUTE, FEMTO SCIENCE) at 100 W for 1 min to activate their surfaces.

The membrane is then carefully aligned and placed onto the hydrogel-embedded microchannel, followed by thermal curing at 120 ℃ for 6 min to achieve robust adhesion. During this process, additional curing of PDMS further stabilizes the hydrogel within the microchannel, ensuring firm attachment during subsequent swelling.

After bonding, the assembled device is aged at room temperature for 24 h to restore the intrinsic hydrophobicity of the PDMS surface.

A schematic illustration summarizing the fabrication process is provided in Fig. S1.

S1.3. Fabrication of diverse applications

The PDMS base structures containing microchannel architectures are fabricated by casting polydimethylsiloxane (Sylgard 184; Vision Lab Sciences) with a base-to-curing agent ratio of 10:1, pre-mixed with a white pigment (Silc Pig™; Smooth-On Inc.), into a custom-designed mold produced via 3D printing (Form 4; Formlabs). The cast structures are cured at room temperature for 24 h and carefully demolded from the molds.

Hydrogel components with various geometries are prepared by casting the synthesized precursor solution into geometry-specific molds, followed by gelation. The formed hydrogels are then embedded into the PDMS microchannels. The assembled PDMS base and hydrogel array are sealed with a trilayer membrane film (thickness ≈ 0.1 mm) to complete device integration. Bonding between the membrane and the PDMS channel is achieved by plasma surface treatment followed by thermal curing at 120 ℃ for 6 min.

For the dew-sensing application, a perforated membrane is prepared by punching nine holes (diameter, 1 mm) at predetermined positions aligned with the hydrogel locations beneath the membrane.

S2. Energy equation modeling

We develop a theoretical model to predict the formation height of hydrobraille dots, governed by the competition between hydrogel swelling and the elastic resistance of the membrane film. The energies stored in the stretched film and the compressed hydrogel can be described using the axial deformation energy equation. In general, the deformation energy is expressed as $e = \sigma A u$, where σ is the axial stress, A is the cross-sectional area over which the stress acts, and u is the axial deformation. According to Hooke's law, the axial stress is defined as $\sigma = E\varepsilon$, where E and ε represent Young's modulus and axial strain, respectively.

In the Hydrobraille system, the overlying membrane film, being highly stretchable, readily extends radially as the hydrogel swells. Under this condition, the effective cross-sectional area over which the stress acts is defined as $A_f \sim R_c h$, where R_c is the radius of the hydrogel-occupied channel, and h is the film thickness. The axial stress in the stretched film can be approximated as $\sigma_f \sim E_f \Delta R_c / R_c$, where E_f is the Young's modulus of the film, and ΔR_c is the radial elongation of the film. The axial deformation is taken as the elongation of the film, $u_f \sim \Delta R_c$. From geometric consideration, $R_c^2 + \delta^2 \sim (R_c + \Delta R_c)^2$, which yields the expression for the radial elongation of the film as $\Delta R_c \sim (R_c^2 + \delta^2)^{1/2} - R_c$, where δ denotes the braille dot height. Combining these relationships, the elastic energy stored in the stretched film can be written as

$$e_f = hE_f \left\{ 2{R_c}^2 + \delta^2 - 2R_c \left({R_c}^2 + \delta^2 \right)^{1/2} \right\}. \quad \text{(S1)}$$

The hydrogel is simultaneously compressed by the overlying film, leading to an equilibrium extrusion height of the braille dot. The cross-sectional area of the swollen hydrogel compressed by film is expressed as $A_h \sim \beta\{R(1+s)\}^2$, where R is the initial radius of the hydrogel, s is the isotropic swelling ratio, and β is a correction factor. We used a bullet-shaped hydrogel geometry with a height equal to the channel depth, d. Since the channel depth scales with the initial hydrogel radius as $d \sim 1.8R$ (see Fig. S2a), the swollen hydrogel height is given by $1.8R(1+s)$. Considering this geometry, axial stress acting on swollen hydrogel is expressed as $\sigma_h \sim E_h \delta^* / \{1.8R(1+s)\}$, where E_h is Young's modulus of swollen hydrogel and δ^* is vertical compression imposed by the membrane. The axial deformation is considered as compression of swollen hydrogel, $u_h \sim \delta^*$, where the vertical compression is defined as $\delta^* \sim 1.8Rs - \delta$. Combining these relationships yields the expression of the energy stored in the hydrogel, which is written as

$$e_h = \beta E_h R(1+s)(1.8Rs - \delta)^2 / 1.8\,. \quad \text{(S2)}$$

By minimizing the total elastic energy of the system with respect to the extrusion height, $\partial(e_f + e_h)/\partial\delta = 0$, we obtain the governing equation for the equilibrium extrusion height,

$$\left\{2hE_f + \beta\frac{2R(1+s)}{1.8}E_h\right\}^2\delta^4 - 4\beta R^2 s(1+s)E_h\left\{2hE_f + \beta\frac{2R(1+s)}{1.8}E_h\right\}\delta^3 +$$
$$\left[\left\{2hE_f + \beta\frac{2R(1+s)}{1.8}E_h\right\}^2 {R_c}^2 + \{2\beta R^2 s(1+s)E_h\}^2 - \left(2hE_f R_c\right)^2\right]\delta^2 - \quad \text{(S3)}$$
$$4\beta R^2 s(1+s)E_h {R_c}^2\left\{2hE_f + \beta\frac{2R(1+s)}{1.8}E_h\right\}\delta + {R_c}^2\{2\beta R^2 s(1+s)E_h\}^2 = 0.$$

where $\beta = 0.6$, introduced as a prefactor to match the theoretical predictions with the experimental measurements. Here, we use the experimentally measured swelling strain $s = 1.5$.

Solving Eq. (S3) with a fixed initial hydrogel radius ($R = 0.333$ mm) at different film thicknesses, h, provides the predicted extrusion heights under various membrane thickness conditions, as shown by the solid line in Fig. 2a. Conversely, solving Eq. (S3) with a fixed film thickness ($h = 0.1$ mm) at different radii (R) gives the theoretically predicted extrusion heights as a function of hydrogel size, shown by the solid line in Fig. 2c. In this analysis, we additionally fix the ratio between the channel radius and hydrogel radius at $R_c \sim 3.5R$, based on the experimentally measured geometric relationship (Fig. S2b).

S3. Finite Element Modeling

We perform finite element simulations using Abaqus/Standard to analyze the deformation of the hydrobraille system. Depending on the symmetry of each configuration, we construct either a 2D axisymmetric model or a 3D half model and solve it with a static general procedure including geometric nonlinearity. We model PDMS, Ecoflex, and polyacrylamide hydrogel as incompressible Mooney–Rivlin hyperelastic solids, and we obtain material parameters by fitting tensile test data (see Supplementary Material S5). We represent hydrogel swelling through an equivalent thermal expansion that induces isotropic volumetric strain. To capture the final deformed geometry, we assign the hydrogel properties of the fully swollen state. A friction coefficient of 0.02 is applied at the interface between the hydrogel and the film [S1]. The primary output is the out-of-plane displacement of the membrane, which we compare with experimental measurements.

The simulation is categorized into two groups based on their objectives and geometrical complexity: (1) parametric analysis of braille dot formation and (2) surface morphing simulation of a flower-shaped tactile graphic.

S3.1. Parametric simulation of braille extrusion

This simulation corresponds to dashed lines in Fig. 2b and Fig. 2c in the main text. To investigate how the extrusion height, δ, depends on film thickness, h, and hydrogel radius, R,

we construct 2D axisymmetric models. The geometry consists of a hydrogel embedded beneath a tri-layer elastic plate. The hydrogel is modeled using CAX4RH hybrid elements, and three plates are modeled using SAX1 elements representing the PDMS-Ecoflex 0030-PDMS tri-layer.

We simulate hygroscopic swelling by applying an equivalent thermal expansion, calibrated to produce the desired strain. The material properties of the hydrogel are fitted to uniaxial tensile test data and assumed to be constant, corresponding to the fully swollen state. For PDMS and Ecoflex 0030, we also fit the parameters to uniaxial tests, and we model all three materials using the incompressible Mooney–Rivlin hyperelastic model. We define contact interaction at the hydrogel–membrane interface with a friction coefficient of 0.02. Mesh convergence is confirmed by refining the mesh until changes in δ were within 2%. The primary simulation output is the vertical deformation of the membrane under a hydrogel hygroscopic strain of 1.5, representing the fully swollen state.

To examine the effect of film thickness (h), (Fig. 2b), simulations are performed at a fixed hydrogel radius, R of 0.33 mm, varying the film thickness from 0.025 mm to 0.5 mm in 0.025 increments. Conversely, to investigate the effect of hydrogel size (Fig.2c), the film thickness, h, is fixed at 0.1 mm, and the hydrogel radius, R, is varied from 0.1 mm to 2.5 mm in 0.1 mm increments. The channel radius, R_c, is varied according to the relationship, $R_c = 3.5\,R$.

S3.2. Simulation of a flower-shaped tactile morphing surface

This simulation corresponds to Figures 3g and 3h and explores the surface transformation of a flower-shaped tactile graphic composed of multiple hydrogel regions. We construct a 3D half model for computational efficiency by exploiting the symmetry of the tactile morphing shape. We embed hydrogels of varying geometries, including dot, line, and area shapes, within a PDMS base layer and cover them with a flexible membrane.

We model each hydrogel using C3D8RH hybrid brick elements and implement swelling through equivalent thermal expansion calibrated to match the experimentally measured hygroscopic strain. We represent the tri-layer plate as a shell structure with S4R elements, corresponding to the PDMS–Ecoflex laminated film. We treat the PDMS channel base structure, which is relatively stiffer and much thicker than the plate, as rigid and model it with R3D43 elements. We set the geometric dimensions of all components to match the experimental configurations and define contact conditions in the same way as in the parametric study simulation.

S4. Extrusion height in various liquid conditions

The swelling dynamics of the hydrobraille system are governed by the diffusion of water into the polymer network. The poroelastic diffusivity D of the hydrogel can be estimated using the relationship $D = E_h k(1 - v)/[\mu(1 + v)(1 - 2v)]$, where k is the permeability (scaling as b^2, with b being the mesh size of the polymer network), μ is the viscosity of solution, and v is the Poisson's ratio [17,18]. Assuming representative material parameters for saturated PAAm hydrogels ($E_h \approx 34$ kPa, $v = 0.486$ [19], $b \sim 10^{-9}$ m [20]) and using the viscosity of water $\mu \approx 10^{-3}$ Pa s, the estimated diffusivity, D, is order of 10^{-10} m^2 s^{-1}. Using a swollen hydrogel height, R_s, on the order of 1.5 mm, the characteristic diffusion time τ can be estimated as $\tau \sim R_s^2/D \sim 1000$ s. This time scale is consistent with the observed saturation behavior in the experiment shown in Fig. 2e, supporting the relevance of the diffusion-based swelling mechanism. Building on this framework, we further examine how the swelling kinetics are influenced by solvent viscosity and temperature.

S4.1. Temporal evolution of extrusion height in various liquid viscosity

We investigate the effect of liquid viscosity on the extrusion height of the hydrobraille system using water-glycerol mixtures as model solutions. In our experiment, the viscosity is systematically tuned by adjusting the mixing ratio of water to glycerol (water:glycerol = 10:0, 7:3, and 5:5), with the corresponding viscosity values summarized in Table S2. Previous studies have established that increasing viscosity reduces effective diffusivity, thereby slowing hydrogel swelling kinetics. Consistent with this trend, our measurements show that the time required for the extrusion height to reach equilibrium increases with liquid viscosity (Fig.S3a).

S4.2. Temporal evolution of extrusion height under different temperatures

We next examine the effect of solution temperature on hydrobraille dot formation using water as the surrounding liquid. In these experiments, the liquid temperature is controlled over a range from room temperature to 60 ℃ using a hot plate, with the exact temperature values indicated in the legend of Fig. S3b. According to prior studies, the diffusivity of hydrogel is inversely related to the viscosity of the surrounding solution. As the temperature of water increases, its viscosity decreases, leading to enhanced diffusivity within the hydrogel network. As a result, the time required to reach the equilibrium extrusion height decreases with increasing temperature: at room temperature, it requires approximately 40 min to reach equilibrium, whereas at 60 ℃, it reaches equilibrium within ~ 15 min, as shown in Fig. S3b.

These results confirm that the swelling dynamics of the hydrobraille system are governed not only by the intrinsic properties of the hydrogel network, but also by the rheological characteristics of the surrounding environment. The ability to tune the swelling speed through external parameters such as fluid viscosity and temperature, in combination with internal material properties including modulus and network structure, provides a versatile design strategy for applications requiring controlled temporal responses.

S5. Mechanical Characterization

We evaluate tensile properties of PAAm hydrogel, Sylgard 184, and Ecoflex 00-30 using a rheometer (HR 20, TA Instruments, tensile mode) or a universal testing machine (5943, Instron). We prepare dumbbell-shaped specimens with an inner width of 10 mm and an inner length of 40 mm, and test Sylgard and Ecoflex samples in their as-cured state without additional swelling or conditioning. For PAAm hydrogels, we cut them into dumbbell-shaped specimens and swell them in deionized water for 5days to reach equilibrium.

During the tensile test, samples with an initial gauge length (l_0 = 40 mm) are stretched at a constant strain rate of 16.6 μm s^{-1}. The tensile stress (σ_t) is calculated as the load force (F) divided by the initial cross-sectional area (A_0), expressed as $\sigma_t = F/A_0$. The tensile strain (ε_t) is determined from $\varepsilon_t = (l - l_0)/l_0$, where l is the final length and l_0 is the original length of the sample. Stress–strain curves of all tested materials are presented in Fig. S5. We obtain Young's modulus (E) from the slope of the stress–strain curve within the initial 5% strain regime, and the values for each material are summarized in Table S3.

S6. Importance of hydrogel in hydrobaille patch for preventing dew run-off

The hydrobraille patch (red) and the perforated PDMS without hydrogels (blue) show similar uncaptured dew volumes in Fig. 5e. However, the two systems differ in their liquid-retention mechanisms (see Fig. S7a). In the perforated PDMS without hydrogels, water is retained within geometric void spaces and remains in a free liquid state. In contrast, the hydrobraille patch absorbs liquid into the crosslinked hydrogel network, where the liquid is effectively immobilized. This difference in retention mechanism influences the stability of the retained liquid. In the perforated PDMS, the liquid can be redistributed or released under external disturbances such as vibration or mechanical perturbation. In comparison, the hydrobraille patch maintains more stable liquid retention due to absorption within the hydrogel network.

The quantitative difference between the two systems can be understood through a volumetric analysis based on the geometries illustrated in Fig. S7b. For the hydrobraille patch, the absorbed liquid volume by a single hydrogel corresponds to the difference between its fully swollen volume (V_s) and its dry volume (V_d). These are given by $V_d = 22\pi R^3/15$ and $V_s = 22\pi[(1+s)R]^3/15$, where R is the initial hydrogel radius and s is the swelling strain. Accordingly, the absorbed volume per hydrogel is $V_a = V_s - V_d$. For the perforated PDMS without hydrogels, liquid is retained only within the geometric void of each perforation, with a volume approximated as $V_p = \pi R_c^2 d$, where R_c and d denoted the radius and depth of the void, respectively. The key quantity determining the performance advantage of the hydrobraille patch over the perforated PDMS is therefore the difference $\Delta V = V_a - V_p$ per unit, which represents the additional liquid volume captured by the hydrogel relative to the void alone.

Using the measured paparmeters (R = 1.8 mm, s = 1.5, R_c = 4.5 mm, d = 3.24 mm), V_a is estimated to be approximately 0.393 mL per hydrogel and V_p approximately 0.206 mL per void, giving $\Delta V \approx 0.187$ mL per unit. With N = 16 hydrogels in the current demonstration, the total additional liquid captured by the hydrobraille patch relative to the perforated PDMS is $N\Delta V \approx 3.0$ mL, which is in close agreement with the experimentally observed difference in Fig. 5e. This consistency indicates that the hydrogel component is the primary contributor to the enhanced water retention capacity of the hydrobraille patch. Since the total additional captured volume scales linearly with the number of hydrogel units ($N\Delta V$), increasing the number of hydrogels directly enhances the water retention capacity of the patch. In the current demonstration, N = 16 is used; scaling to a larger area by increasing N is therefore expected to yield proportionally greater water capture (Fig. S7c). This suggests strong potential for large-area moisture management applications, where a higher density of hydrogel units can be employed to achieve enhanced condensation suppression.

S7. Effect of liquid volume on extrusion height

We investigate the effect of liquid volume on the extrusion height by introducing a nondimensionalized variable, liquid fraction $\zeta = V_l/(V_s - V_d)$, where V_l is the liquid volume, V_d is the dry hydrogel volume, and V_s is the fully swollen hydrogel volume (see Fig. S7b). The liquid fraction ranges from 0 to 1, where $\zeta = 0$ corresponds to the completely dry state and $\zeta = 1$ corresponds to full saturation of the hydrogel. Based on the hygroscopic strain formulation for porous materials, the swelling strain can be expressed as a function of the liquid fraction as $s(\zeta) \sim \alpha_h \varphi \zeta$, where α_h is the hygroscopic swelling coefficient and φ is the void fraction of

the polymer network estimated as $\varphi \sim (V_s - V_d)/V_s$. Using the measured swelling strain (s = 1.5), the void fraction of the hydrogel used in this study is estimated to be $\varphi \sim 0.936$.

To quantify the relationship between liquid volume and extrusion height, we incorporate (ζ) into the governing equation for the equilibrium extrusion height (Eq. S3), thereby expressing the extrusion height as an explicit function of the liquid fraction. Solving the combined equations with fixed parameters (R = 0.333 mm, h = 0.1 mm, and R_c = 1.5 mm) gives us the predicted extrusion heights for ζ ranging from 0 to 1 (see Fig. S8). As the liquid fraction (ζ) increases from 0 (dry) to 1 (full saturation), the extrusion height increases gradually and approaches its equilibrium value at ζ = 1.

We further examine the effect of the hygroscopic swelling coefficient α_h on the extrusion height, as shown by the different curves in Fig. S8. As α_h increases, the swelling strain for a given liquid fraction becomes larger, leading to a correspondingly higher extrusion height. This result indicates that both the amount of absorbed liquid and the intrinsic swelling characteristics of the hydrogel jointly determine the resulting tactile protrusion height.

S8. Relationship between swelling ratio and extrusion height

We investigate the relationship between the hydrogel swelling ratio and the extrusion height using the mechanical model, Eq. (S3). By solving Eq. (S3) under fixed conditions (R = 0.333 mm, h = 0.1 mm, and R_c = 1.5 mm) for different values of swelling ratio s, we obtain the predicted extrusion heights as a function of s, as shown in Fig. S9.

As the swelling ratio increases from s = 0 (dry state), the extrusion height increases in a nonlinear manner, with a steeper rate of increase at lower values of s. This behavior reflects the mechanical equilibrium between the expanding hydrogel and the elastic resistance of the overlying membrane, where the membrane becomes increasingly resistant to deformation as the hydrogel approaches full saturation. For the hydrogel used in this study, at s = 1.5, the extrusion height reaches its equilibrium value (dashed line in Fig. S9).

References

[S1] J. Kim, G. Zhang, M. Shi, and Z. Suo, “Fracture, fatigue, and friction of polymers in which entanglements greatly outnumber cross-links”, *Science* **374**, 212–216 (2021), https://doi.org/10.1126/science.abg6320

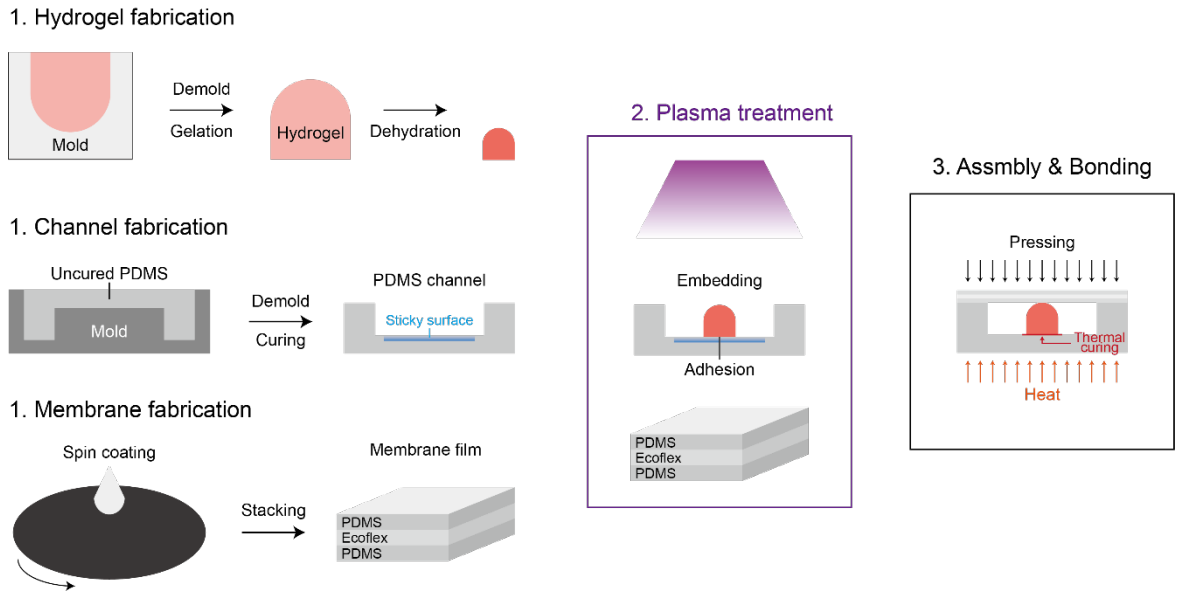

Fig. S1. Schematic illustration of the hydrobraille fabrication process, including hydrogel preparation, channel fabrication, and trilayer membrane fabrication. The hydrogel is embedded in the PDMS microchannel while the PDMS remains partially cured, followed by plasma treatment and final thermal bonding with the membrane.

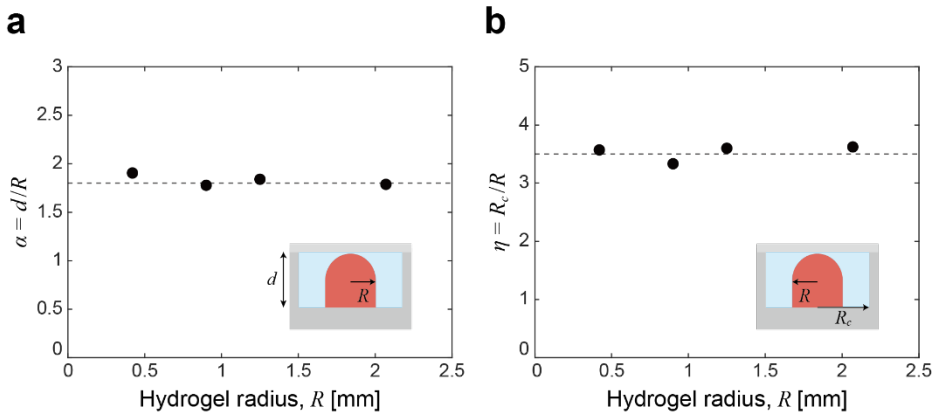

Fig. S2. Geometrical relationships in the hydrobraille. **(a)** Experimentally measured ratio of channel depth, d, to initial hydrogel radius, R. The dashed line indicates the relation $d \sim 1.8\ R$. **(b)** Experimentally measured ratio of channel radius, R_c, to initial hydrogel radius, R. The dashed line indicates the relation $R_c \sim 3.5\ R$.

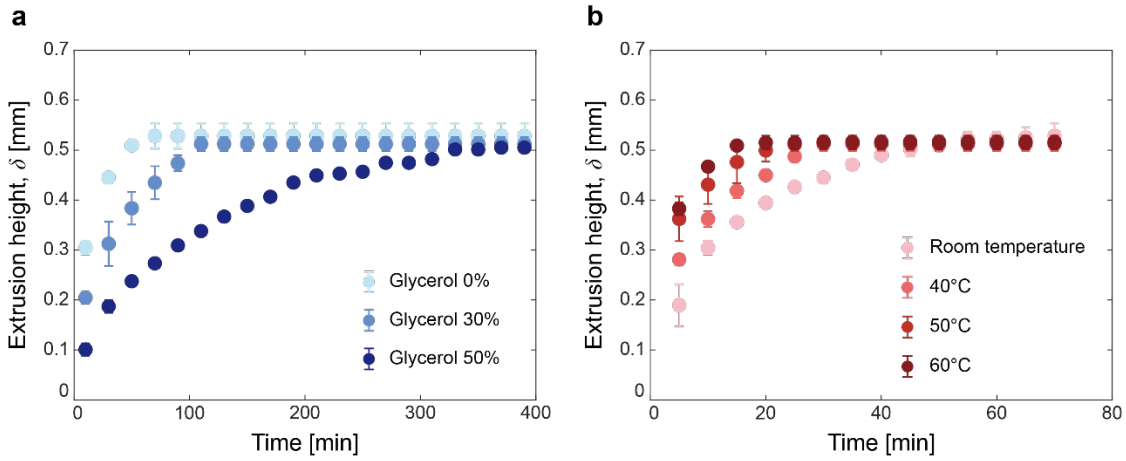

Fig. S3. Effects of the surrounding liquid environments on hydrobraille. **(a)** Temporal evolution of extrusion height in liquids of varying viscosity. **(b)** Temporal evolution of extrusion height in water at different temperatures.

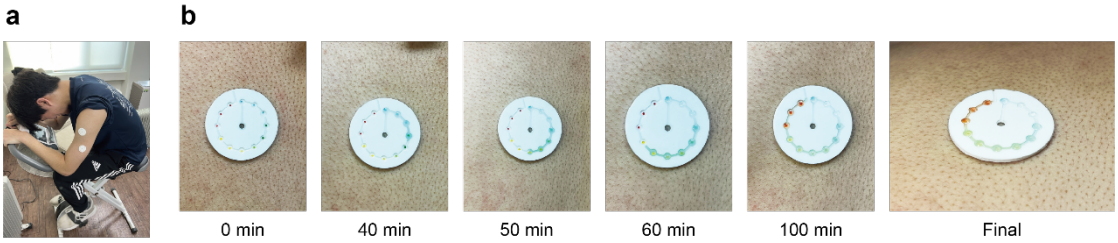

Fig. S4. Experimental validation of the sweat-capturing patch. **(a)** Validation method. **(b)** Time-lapse experimental images showing sweat capture and subsequent hydrogel swelling.

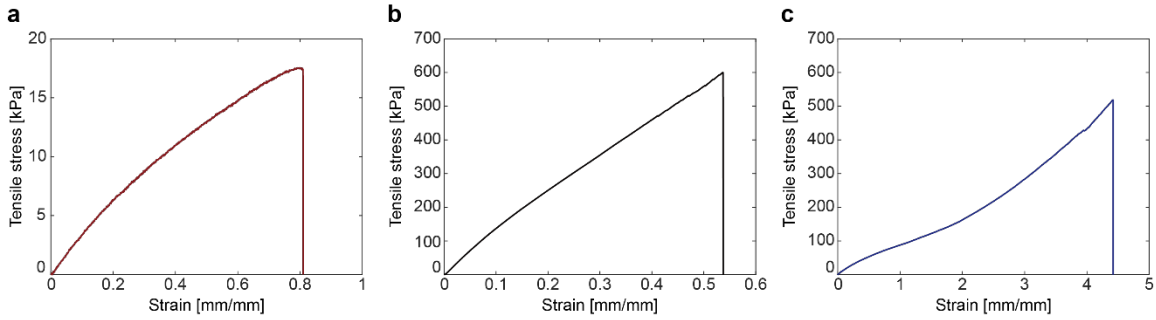

Fig. S5. Strain-stress curves. **(a)** PAAm hydrogel tensile test graph. **(b)** PDMS tensile test graph. **(c)** Ecoflex 00-30 tensile test graph.

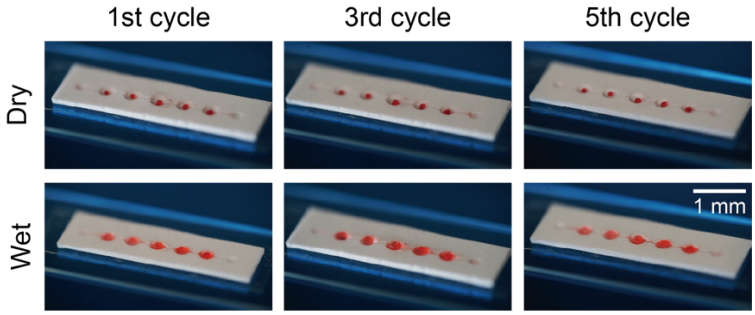

Fig. S6. Repeatable operation of hydrobraille (R = 0.333 mm, h = 0.1 mm, and R_c = 1.5 mm).

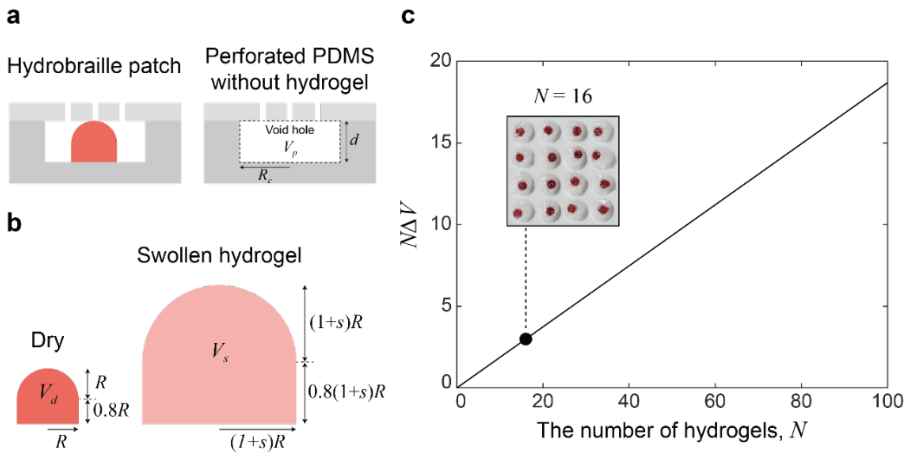

Fig. S7. (a) Schematic illustrations of the hydrobraille patch and the perforated PDMS without hydrogels used in the dew prevention application. (b) Schematic illustration of the hydrogel in the dry and fully swollen states. (c) The total additional liquid captured by the hydrobraille patch relative to the perforated PDMS in various N.

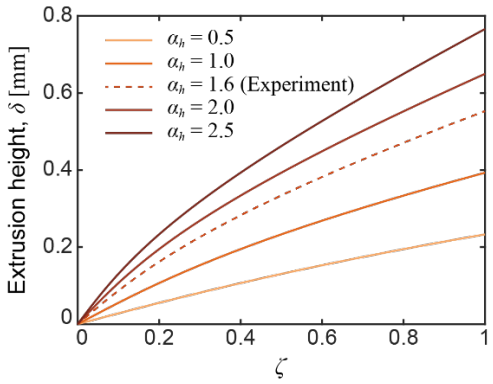

Fig. S8. Predicted extrusion height as a function of the liquid fraction (ζ) for different values of the hygroscopic swelling coefficient (α_h). The dashed line corresponds to the hydrogel used in this study.

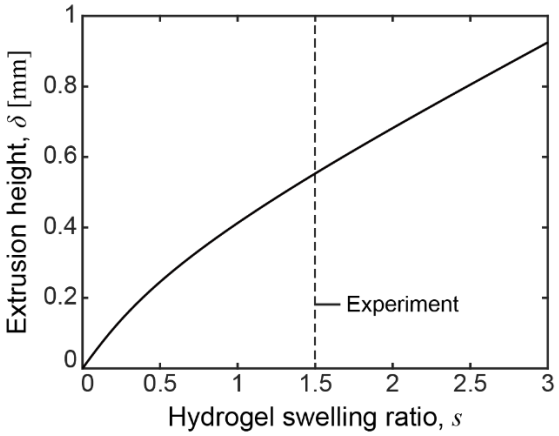

Fig. S9. Extrusion height as a function of swelling ratio, s, under fixed conditions (R = 0.333 mm, h = 0.1 mm, R_c = 1.5 mm). The solid line indicates theoretical predictions obtained by solving Eq. (S3). The dashed line corresponds to the hydrogel used in this study (s = 1.5).

Spin-coating speed [rpm]	Film thickness, h [μm]
4,000	50
3,000	100
1,900	150
1,300	200
1,000	250
900	300
800	350
740	400
700	450

Table S1. Spin coating speeds for membrane fabrication. Each material is spin-coated for 30 s. Two PDMS layers and one Ecoflex layer are combined to form a single membrane film with a thickness, h.

Liquid	Viscosity, μ [Pa s]
Water	0.001
Glycerol 30 wt%	0.0022
Glycerol 50 wt%	0.0051

Table S2. Viscosities of Liquids.

Material	Young's modulus, E [kPa]
PAAm hydrogel	34
Sylgard 184	1,269
Ecoflex 00-30	160

Table S3. Young's modulus of PAAm hydrogel, Sylgard 184, and Ecoflex 00-30.